Supporting Information: Spin States Protected from Intrinsic Electron-Phonon-Coupling Reaching 100 ns Lifetime at Room Temperature in $MoSe_2$

Manfred Ersfeld,[1] Frank Volmer,[1] Pedro Miguel M. C. de Melo,[2,3] Robin de Winter,[1] Maximilian Heithoff,[1] Zeila Zanolli,[3,4,5] Christoph Stampfer,[1,6] Matthieu J. Verstraete,[2,3] and Bernd Beschoten[1]

[1] *2nd Institute of Physics and JARA-FIT, RWTH Aachen University, D-52074 Aachen, Germany*
[2] *nanomat/Q-mat/CESAM, Université de Liège, B-4000 Sart Tilman, Liège, Belgium*
[3] *European Theoretical Spectroscopy Facilities (ETSF)*
[4] *Catalan Institute of Nanoscience and Nanotechnology (ICN2), CSIC and BIST, Campus UAB, Bellaterra, 08193 Barcelona, Spain*
[5] *Institute for Theoretical Solid State Physics, RWTH Aachen University, D-52056 Aachen, Germany*
[6] *Peter Grünberg Institute (PGI-9), Forschungszentrum Jülich, D-52425 Jülich, Germany*

I. TEMPORAL CHANGES IN SPIN LIFETIME AT ROOM TEMPERATURE

We note that the room temperature TRKR signal of sample M1 seen in Fig. 1(b) of the main manuscript did not decrease continuously with each successive measurement, but rather decreased and increased without discernible pattern. As such kind of change in device properties may be explained by different kind of adsorbates on top of the flake, we tried to keep the vacuum conditions for each of our measurements as reproducible as possible. Unfortunately, the two-dimensional nature of the TMD flake demands technological requirements that are beyond the possibilities of our setup. In surface science it is a well-known fact that reproducible conditions can only be achieved under ultra-high vacuum conditions (below 10^{-9} mbar). In the experiment we used a continuous flow cryostat that can be pumped down at room temperature to a base pressure of 10^{-6} mbar. From a surface science point of view, such conditions are "dirty" (it is equal to a monolayer formation time of contaminating gas species on top of a clean surface of only 1 s). It is known that air-born hydrocarbons cover the surface of 2D materials once they were exposed to air.[1,2] Even under vacuum conditions the binding energy of long-chained hydrocarbons leads to desorption temperatures above RT.[1,3] But as our cryostat cannot be baked-out at high temperatures, we do not have control over the residual gas composition, which e.g. condenses on the sample surface during a cool-down.

As the longest spin lifetimes exceed by far the adjustable delay time (which is limited by the laser repetition interval of 12.5 ns), the question arises how reliable the fitted lifetimes are as soon as they are in the 100 ns range. In Fig. S1 of this supplemental material we fitted one of the room temperature measurements on sample M1 with spin lifetimes on the order of 100 ns by a two-exponential decay function and fixed the longer of the two spin components either to 70 ns or 100 ns, respectively. For an assumed spin lifetime of 70 ns the majority of data points lie either below or above the dashed line for time delays lower or higher than $\Delta t = 6$ ns, respectively. Because of this systematic behavior of the residuals, the actual lifetime has to be longer than 70 ns. We repeated such fits with increasing but fixed values of the spin lifetime. At $\tau_s =$ 100 ns the signal-to-noise ratio of the curve masked any possible systematic trend in the residuals. Hence, the true spin lifetime has to be at least 100 ns.

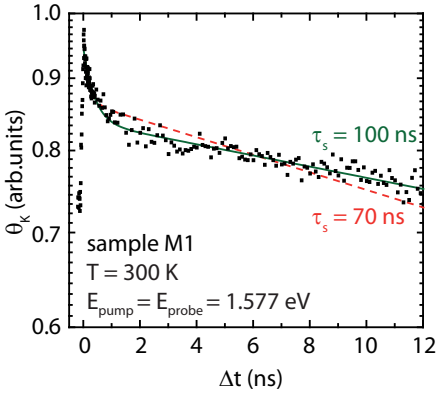

FIG. S1. Time resolved Kerr rotation curve of sample M1 which shows a decay time of around 100 ns at room temperature. Fits were done by fixing the longer of two decay times of a two-exponential decay function to either 70 ns or 100 ns.

II. CHALLENGES IN THE MEASUREMENT OF THE RT SPIN SIGNAL

We note that the Kerr rotation amplitude of the RT spin signal in sample M1 is only in the order of some μrad, which is significantly lower than the spin signal at lower temperatures, where the Kerr rotation reaches tens of μrad. However, most likely due to the 2-dimensional character of the TMD, even the amplitudes of the low-temperature spin signal fall short to typical Kerr rotation values measured e.g. in GaAs or ZnO where values of several hundreds of μrad or even mrad can be measured.[4,5]

There are two challenges with these small amplitudes: First, a good adjustment of all optical elements and long integration times are needed to obtain a decent signal-to-noise ratio. A single delay scan at RT (like it is shown in Fig. 2(b) of the main manuscript) takes at least one hour. Now it is important to note that changes in the spin signals

predominantly occur at higher temperatures, whereas the spin properties are very stable at low temperatures.[6] As mentioned above, this can be explained by adsorbates on the TMD flake which condense at cryogenic temperatures, but can freely adsorb and desorb at higher temperatures. The unstable spin properties at higher temperature combined with the required long acquisition times for a single delay scan does not allow to measure e.g. consistent Kerr resonance curves (i.e. probe scans).

The other challenge considering the small Kerr rotation signal is a possible small background in the Kerr rotation data. A spurious electronic signal responsible for such a background can, e.g., be generated by the balanced diode bridge we use for our optical Kerr measurements.[7] Because of the finite common mode rejection of the used differential amplifier in such an optical bridge, each balanced diode bridge will output a small spurious differential signal. Depending on the exact adjustment of the whole laser system (see schematic setup in the supplemental material of Ref. 6) and the used settings of lock-in and voltage amplifiers, we normally observe a background signal up to several hundreds of nrad. We note that such a small background signal can be easily overlooked if the actual spin signal is e.g. several hundreds of μrad large. However, in our case (in which the RT spin signal is only several μrad large) such a constant background can have a non-negligible influence on the determined spin lifetime. This is especially the case if the spin lifetimes exceed the measurable delay time.

If the signal was showing, e.g., spin precession or any other kind of magnetic field dependence, such a background could in principle be determined at high enough magnetic field strengths. However, our samples do not show any magnetic field dependence. Therefore, we determined the background signal by reference measurements in which we moved the sample approximately 100 μm away from the laser spots and measured the resulting signal on the Si/SiO_2 wafer. The determined background was subtracted from all subsequent measurements.

We note that the above mentioned spurious signals from the electronics can be seen as constant over the measurement time and therefore cannot explain the clear, reproducible jump at zero delay and the exponential decay in our Kerr data. Furthermore, we regularly checked if the signal, which we identified as the spin signal, changes sign by inverting the helicity of the pump laser. Additionally, we note that the spin signal vanishes if the pump beam is linearly polarized or if either the pump or probe beam is individually blocked. Therefore, we exclude other laser-induced effects as the origin of the long-lived signal.

III. FITTING OF THE KERR ROTATION CURVE

The Kerr rotation signal $\Theta_K(t)$ for all samples were fitted over the whole temperature range by a bi-exponential fit function of the form:

$$\Theta_K(t) = \sum_{i=1}^{2} A_i \cdot \exp\left(-\frac{t}{\tau_{s,i}}\right), \qquad (1)$$

where A_i are the amplitudes and $\tau_{s,i}$ are the spin lifetimes for each component. As the absolute value of the Kerr rotation is very sensitive to the alignment of the laser system in general and the overlap of pump and probe beam in special, great care was taken for the temperature dependent measurements shown in Figs. 1(c), 3(a), and 3(b) of the main manuscript. For each temperature, we spatially mapped both Kerr signal and reflectivity over the whole flake to guarantee the probing of the same spot on the sample. This is important as thermal expansion of the cryostat changes the relative position of the sample in respect to the laser beams. Furthermore, for each temperature we checked that pump and probe beam were in good overlap to each other. Nevertheless, unavoidable slight variations in the probed location of the sample and minimal variations in the overlap cannot be completely avoided and are the most likely explanation for the scattering of the Kerr amplitude in Fig. 1(c) of the main manuscript.

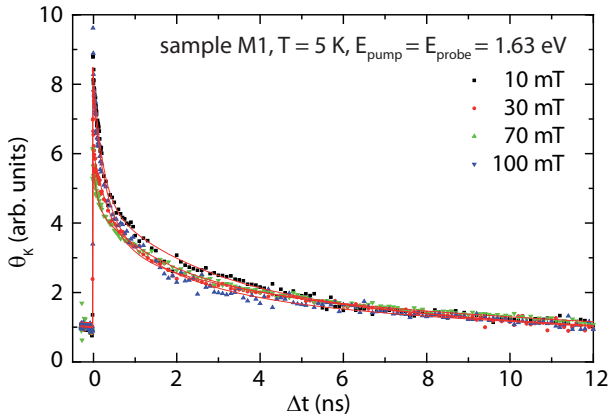

FIG. S2. TRKR curves of sample M1 in the trion regime at 5 K for different magnetic fields applied in-plane to the $MoSe_2$ flake. Red curves are fits according to a multi-exponential fit function.

IV. MAGNETIC FIELD DEPENDENT MEASUREMENTS

In Fig. S2 of this supplemental material we show TRKR curves of sample M1 in the trion regime at 5 K for different magnetic fields. The field was applied in-plane to the $MoSe_2$ flake and thus transverse to the spin direction of the optically generated spin states. We note that the cryostat slightly moves when applying a magnetic field. This is important as PL and Kerr-measurements already demonstrated that a TMD flake can have spatially varying optical properties.[8] This may explain the marginal change

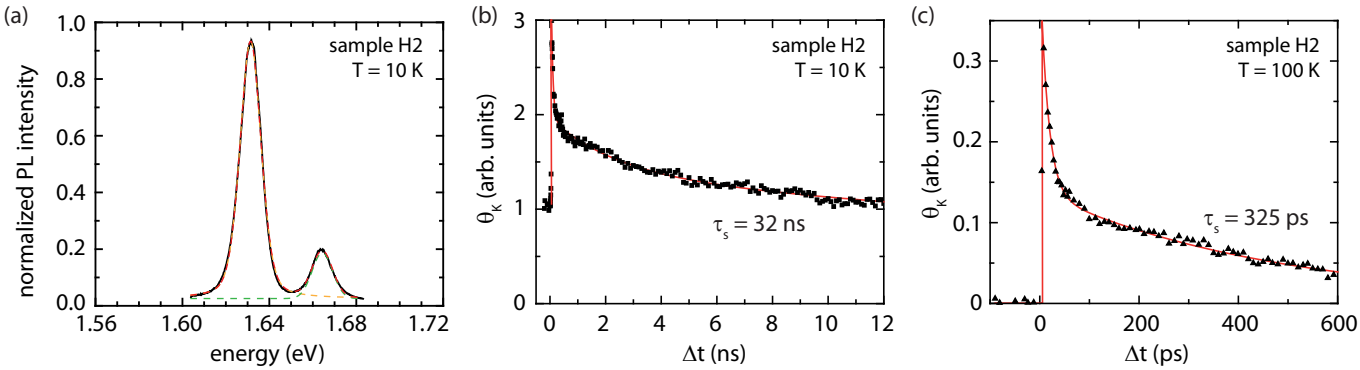

FIG. S3. (a) Photoluminescence spectra for sample H2 at $T = 10$ K. The red dashed line is the sum of two Voigt functions fitted to the exciton and trion peak (green and orange dashed line, respectively). (b) and (c): Time-resolved Kerr rotation curves of sample H2 at $T = 10$ K and $T = 100$ K, respectively. The red lines are fits to a bi-exponential function.

between the curves within the first few ns, i.e. in the short-lived spin signal of the multi-exponential fit. On the other hand, the long-lived spin signal, which is the main focus in our main manuscript, shows no changes as a function of applied magnetic field and, hence, the curves are in good agreement to each other for time delays larger than $\Delta t = 5$ ns.

V. PL AND KERR DATA FOR SAMPLE H2

In Fig. S3 we show both the photoluminescence data at 10 K and the TRKR curves for both 10 K and 100 K for sample H2. The measurement conditions are identical to the one given in the main manuscript for the other samples. Similar to samples H1a and M2a in Figs. 3(a) and 3(b) of the main manuscript, the spin lifetime exponentially decays towards higher temperatures. For this sample, no long-lived spin state with inverted sign can be measured within the resolution of our setup.

VI. PEAK POSITIONS OF NEUTRAL EXCITONS

As mentioned in the main manuscript, the sample with the long-lived RT spin signal (sample M1) exhibits an exciton peak position at quite high energies at 1.665 eV. This energy is higher than the vast majority of values reported in literature as can be seen in Tab. S1. It was shown in several studies that either doping,[9–11] strain,[12–14] or the change of the dielectric environment by encapsulation with hBN[15,16] can be associated with a red-shift of the exciton peak. As no sample except for H1b is in contact with hBN, and all samples are put on Si/SiO_2 substrates, we exclude the dielectric environment as a reason for the large blue-shift: the high exciton energy of sample M1 is therefore indicative of low overall doping and strain.

TABLE S1. Reported values in literature about the exciton peak position in photoluminescence measurements at low temperatures in case of $MoSe_2$ on different substrates

reference	sample/substrate	exciton energy (eV)
10	hBN/$MoSe_2$/hBN	1.630
16	hBN/$MoSe_2$/hBN/SAM	1.640
9	hBN/$MoSe_2$/hBN	1.642
17	$MoSe_2$ Ti doped/SiO_2	1.648
17	$MoSe_2$/h-BN/SiO_2	1.648
16	hBN/$MoSe_2$/hBN	1.650
15	hBN/$MoSe_2$/hBN	1.652
15	$MoSe_2$/hBN	1.655
18	$MoSe_2$/SiO_2	1.655
19	$MoSe_2$	1.655
16	$MoSe_2$/SiO_2	1.657
17	$MoSe_2$ undoped/SiO_2	1.658
17	$MoSe_2$/Au/SiO_2	1.658
20	$MoSe_2$/SiO_2	1.658
21	$MoSe_2$/SiO_2	1.658
17	$MoSe_2$/SiO_2	1.660
15	$MoSe_2$/SiO_2	1.660
17	$MoSe_2$/SiO_2	1.662
22	$MoSe_2$/sapphire	1.665
23	$MoSe_2$/SiO_2	1.667

VII. GROUND STATE AND BAND STRUCTURE

Electronic ground state properties were computed using Density Functional theory (DFT) with the fully-relativistic pseudo-potentials generated by the ONCVPSP code[24] and stored in the Pseudo-Dojo repository[25]. A lattice parameter of 3.28 Å was used. Both the in-plane cell and the positions of the atoms were relaxed. The final distance between the Mo and Se atoms was 2.51 Å and the angle defined by the Se-Mo-Se atoms was 81.84°. The

ground state was computed with a 24 by 24 k-point grid which was then used to compute the databases on a 30 by 30 mesh. A DFT band gap of 1.40 eV was obtained, with the lifting of the degeneracy in the top valence bands at K due to spin-orbit coupling being 0.19 eV. The energy split for the bottom conduction bands at K, also due to spin-orbit, was 0.02 eV. The resulting DFT band structure is shown in red in Fig. S4.

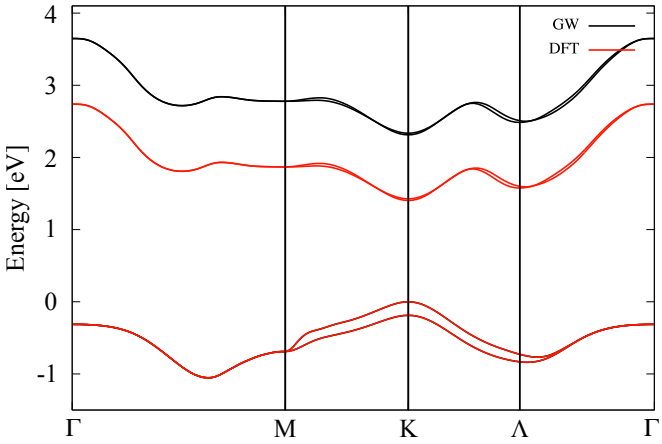

FIG. S4. DFT (red) and G_0W_0 (black) corrected bands for the $MoSe_2$ monolayer computed on a 30 by 30 k-point grid and plotted along the optical path. The G_0W_0 calculation changes the band gap at K from 1.40 eV to 2.34 eV.

To correct the band gap we performed a G_0W_0 calculation using the `Yambo` code[26]. A total of 240 bands and a cutoff of 2000 mHa were used to compute the screening, while 200 bands were needed for the Green's function and a cutoff of 6 Ha was used for the exchange component of the self-energy. The result was a scissor operator of 0.94 eV which was applied to the band structure, as shown in black in Fig. S4. For the remaining of this work, we will label the bands as v1, v2, c1, and c2, referring to the first and second valence bands, and the first and second conduction bands, respectively and in increasing energy.

VIII. OPTICAL ABSORPTION

To compute the absorption spectrum we need to go beyond G_0W_0 and include excitonic effects. This was also done with the `Yambo` code via the Bethe-Salpeter equation (BSE). The screening was computed within the COHSEX approximation and required a cutoff of 2000 mHa and 120 bands, while the exchange part needed a cutoff of 10 Ha. In the building of the kernel the top two valence and the bottom two conduction bands were used. The resulting absorption spectrum is shown in Fig. S5. There we can observe the first two main peaks at 1.69 eV and at 1.90 eV, respectively. The energy difference between the two peaks is 0.21 eV, which is consistent with the spin-orbit splitting of the bands at K.

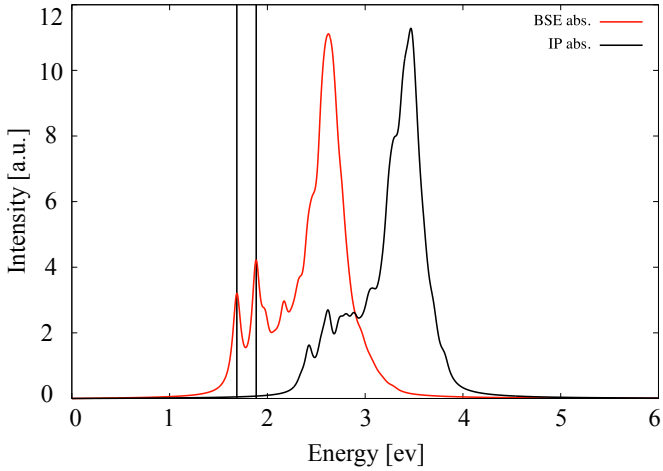

FIG. S5. G_0W_0 corrected (black) and BSE (red) absorption spectrum for the $MoSe_2$ monolayer computed on a 30 by 30 k-point grid. The vertical black lines indicate the positions of the first two excitons, A and B, at 1.69 eV and 1.90 eV respectively, consistent with the computed spin-orbit splitting. The binding energies for the A exciton is 0.66 eV and 0.44 eV for the B exciton.

IX. REAL-TIME DYNAMICS

Our approach to real-time dynamics is based on the Non-equilibrium Green's function (NEGF) formalism and in solving an approximated form of the Baym-Kadanoff equations (BKE)[27–30] for the single-time density matrix $\rho(t)$. The BKE can be written as[27–30]

$$\partial_t \rho_i(t) = \partial_t \rho_i(t)|_{\rm coh} + \partial_t \rho_i(t)|_{\rm coll}, \qquad (2)$$

where $\partial_t \rho_i(t)|_{\rm coh/coll}$ refer to the coherent/collision terms of the dynamics, respectively. Here $\rho(t)$ is expressed on a Kohn-Sham basis for electron-hole pairs, so $i = \{n, n', \mathbf{k}\}$, where n and n' are spinorial band indices and $\mathbf{k}$ is the crystal momentum. The coherent term in Eq. (2) contains the interaction with the laser field and coherent correlation effects. It can be written in a compact form as

$$\partial_t \rho_i(t)|_{\rm coh} = \Delta\epsilon_i \rho_i(t) + \\ + \left[\Delta\Sigma^{Hxc}(t), \rho(t)\right]_i + \left[U(t), \rho(t)\right]_i . \qquad (3)$$

Here, $\Delta\epsilon_i = \epsilon_{n\mathbf{k}} - \epsilon_{n'\mathbf{k}}$ is the energy difference between the quasi-particle energies of the system at equilibrium. The second term on the right-hand-side, $\Delta\Sigma^{Hxc}$, accounts for the change in the Hartree potential and the exchange-correlation self-energy at a given time t, while the last term includes the interaction with the laser field. The latter is given by $U(t) = -\Omega \mathbf{E}(\mathbf{t}) \cdot \mathbf{d_i}$, where Ω is the volume of the unit cell, $\mathbf{E}(\mathbf{t})$ the time-dependent electric field, and $\mathbf{d_i}$ the matrix element of the dipolar moment[31]. While the external electric field drives the excitation of the carriers, the change in the Hartree and exchange-correlation self-energies accounts, in linear order, for the electron-hole interaction by including excitonic effects.

Relaxation of carrier populations is driven by the $\partial_t \rho_i(t)|_{\text{coll}}$, where the important mechanisms for valley scattering are included. It can be written as

$$\partial_t \rho_i(t)|_{\text{coll}} = \sum_I \Big[-\gamma_i^{(e,I)}(t,T)\rho_i(t) + \\ + \gamma_i^{(h,I)}(t,T)\bar{\rho}_i(t) \Big] \quad (4)$$

where $\bar{\rho}_i = \delta_{n,n'} - \rho_i$. The sum runs over an index I, which accounts for all three possible scattering mechanisms: electron-phonon ($I = e-p$), electron-electron ($I = e-e$), and electron-photon ($I = e-\gamma$). The generalised non-equilibrium time-dependent lifetimes γ_i contain the scattering information coming from the Feynman diagrams. A derivation of Eq. (2) and the specific form of these non-equillibirum lifetimes can be found in Ref. 27. Once the evolution in time of the density matrix is computed, we can proceed to the calculation of optical properties. This is done by extracting the time-dependent occupations of the electronic levels at a given time t, $f_{n\mathbf{k}}$, which are the diagonal elements of the density matrix, i.e., $f_{n\mathbf{k}}(t) = \rho_{nn\mathbf{k}}(t)$. The main reasoning behind this is that measurements are performed at a point in time in which the initial dephasing effects induced by the laser pump have vanished already[27–30]. As such, we can easily compute whichever quantity necessary if it can be expressed as a function of the time-dependent occupations and energy levels[27–30].

X. THE ELECTRON-PHONON SCATTERING MECHANISM

We performed *ab initio* time-dependent simulations on a $MoSe_2$ monolayer using a right-hand circularly polarised laser tuned to the energy of the A exciton (1.69 eV) for temperatures of 5 K, 20 K, 40 K, 60 K, 100 K, and 300 K. The laser FWHM and intensity are set to the ones used in the experimental setup. In Fig. S6 we show the evolution in time of the Oz component of the system's magnetisation (M_z) in time, for each temperature.

There is a visible change in the time evolution of the magnetisation when temperature goes from 40 to 60 K, with M_z no longer reversing signal in the latter. This magnetisation results from an imbalance between the electron and hole populations in the K and K' valleys. In Fig. S7 there are snapshots of the these populations in the band structure at 3 ps, 3.5 ps, 4 ps, and 4.5 ps for 40 K and 60 K, together with the change in time of the populations of the bands at each valley. There we see that the creation of pairs in the K valley (due to the laser pump) happens at a time scale close to that of the scattering of carriers towards the K' valley. This similarity in the time scales makes it difficult to understand how each process, excitation and scattering, contributes to overall change in behaviour of the magnetisation, so the two of them need to be picked apart.

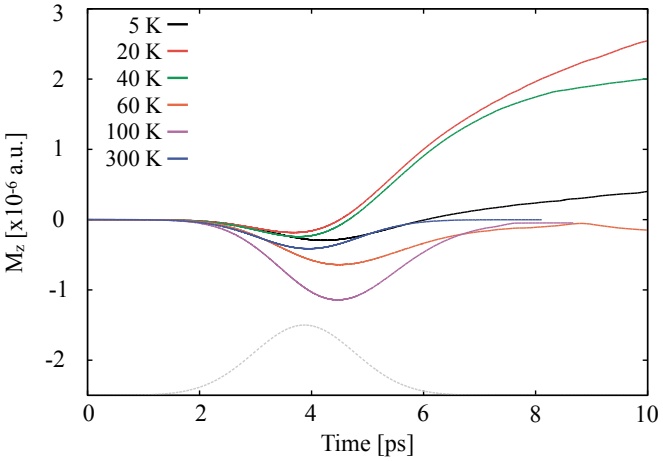

FIG. S6. Evolution in time of the magnetisation along Oz of the $MoSe_2$ monolayer due to the laser pump, for 5 K (black), 20 K (red), 40 K (green), 60 K (orange), 100 K (purple), and 300 K (blue). Profile of laser intensity shown with grey dashed line.

To do so we performed the two types of tests: one in which only the laser field was active and there was no electron-phonon scattering; and another where an electron-hole pair is created artificially and then allowed to interact with the phonon bath.

The effects of the laser pump acting alone on the $MoSe_2$ are represented in Fig. S8. As expected, the laser creates carriers only in the K valley, although not only bands v2 and c1 are populated, but also bands v1 and c2. Such effect has already been reported in literature[32]. Changes in the screening due to promotion of electrons to conduction states induce a renormalisation of the excitonic energies, such that the laser pulse is now capable of promoting electrons up from v1. Then spin and angular momentum selection rules ensure that these electrons are moved to the c2 band.

Taking into account these results we devised the second set of tests to study the effects of the electron-phonon dynamics. Here electrons are promoted "by-hand" from the valence to the conduction states at K exactly in three separate cases (which had to be consistent with the selection rules): from v2 to c1; from v1 to c2; and from v2 to c1 together with the promotion of an electron from v1 to c2. This way we could study how the phonons would affect the carriers created by the laser in a controlled and isolated fashion.

In Figs. S9 to S11 we show the evolution in time of the valley band electron and hole populations for the three test cases with the artificially created excited states. These are evaluated by adding the occupations of each state of a given band that lie in a vicinity of either K or K'. The corresponding evolution in the magnetisation is represented in Fig. S12.

In all three cases it is possible to conclude the following: while both the scattering of electrons and holes is affected by temperature, it is the electrons that suffer the greatest

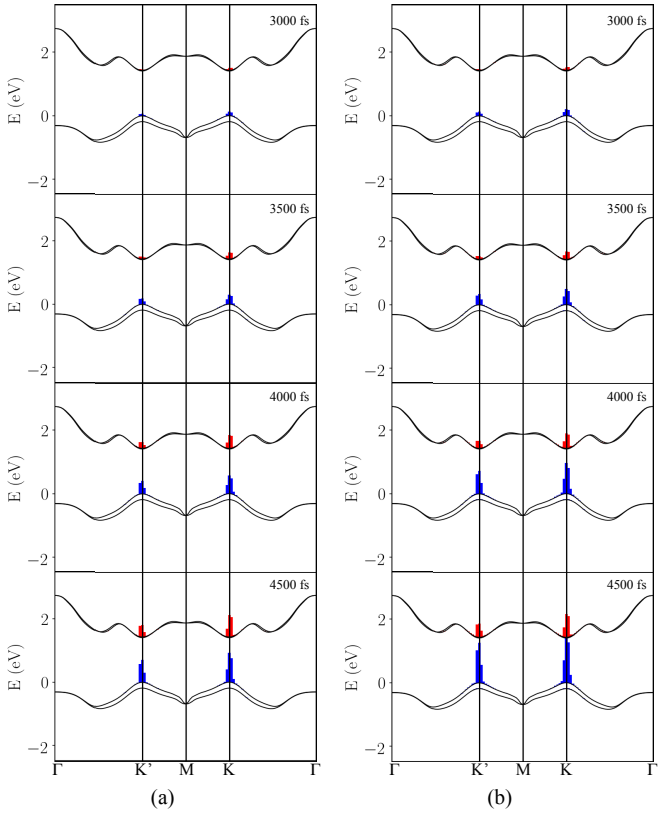

FIG. S7. Time snapshots of electron (red) and hole (blue) occupations at 40 K [(a)] and 60 K [(b)] under the effects of the external laser field.

changes in scattering rates. At 40 K the dominant scattering mechanism for electrons in the conduction states is phonon induced spin flip, due to $\mathbf{q} = 0$ phonons. In Fig. S9 (a) this visible in the changes of the population of the c1 band at K. Its variation in time is less pronounced than that of the holes in band v2 at K. This is understandable, since in order to move to c2, electrons would need to absorb a phonon, but these are scarcely populated at low temperatures. In Fig. S10 (a), as we promote electrons to c2 at K', they can scatter more easily to c1, since this would involve emitting a phonon instead of absorbing one. As the temperature increases, electron scattering to other regions of the Brillouin zone becomes possible. Electrons will then disperse throughout the conduction bands faster than the holes, even staying almost completely outside the K and K' valleys. Hence, the very low populations at 3 ps in Figs. S9 (c) and S10 (c).

The immediate consequence of this change in the scattering rates of electrons relatively to the holes is visible in Fig. S12 a). At 20 K and 40 K the holes move faster than the electrons towards K, so the remaining contribution to the magnetisation will come from electrons which remain stuck in c1 at K. Their magnetic and spin quantum numbers ($m = -1$ and $m_z = -1$) results in a overall negative signal for the magnetisation. As the temperature increases it is the holes which contribute to the overall

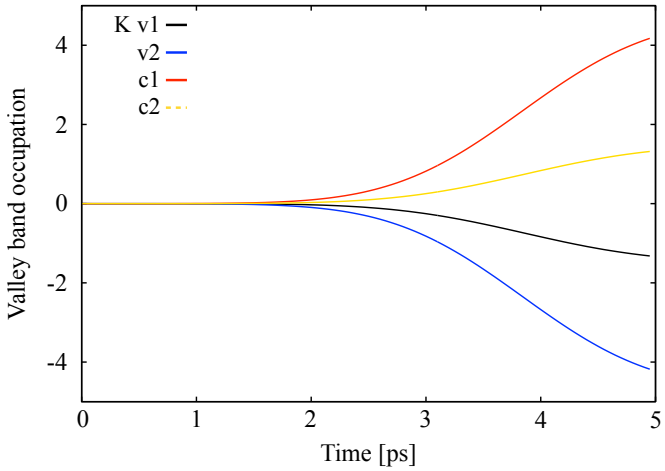

FIG. S8. Evolution in time of the valley band populations at the K valley due to the laser field only. Here hole populations are represented as negative so that there is no overlap between lines representing electron and hole populations.

magnetisation with their spin and angular momentum ($m = 0$ and $m_z = -1$), thus leading to an overall positive signal.

Regarding the hole scattering in Fig. S10, it is visible that the holes created in v1 at K scatter almost equally to v2 at both K' and K and that this scattering mechanism is not altered significantly due to changes in temperature[33]. The overall changes in the magnetisation are visible in Fig. S12 b). At low temperatures electron relaxation is dominated by phonon induced spin flip, with electrons remaining trapped in K. This induces a change from states that are dominantly spin-up to states that are dominantly spin-down, inverting the signal of the magnetisation. At higher temperatures electrons are no longer trapped in K, so the holes are again the only contributors to the magnetisation, which reaches zero as the populations in both valleys equalise.

The convolution of these two effects, phonon-induced spin-flip and intra-valley scattering, is represented in Fig. S11 and in Fig. S12 (c). As stated before, here two electron-hole pairs are created, one in bands v2 and c1, and another in bands v1 and c2, both at K. At 40 K [Fig. S11 (a)] the intra-valley scattering is the dominant process for electron relaxation, even increasing the population of band c1 at K. The same effect is visible in the hole populations, where the holes created in v1 at K scatter into band v2 at both K and K', thus delaying the point at which both valleys would achieve equal populations of holes. By increasing the temperature, inter-valley scattering becomes more prominent for the holes and they are allowed to balance the populations in both valleys.

The analysis of the effects from the laser pump and the phonon induced scattering allows us to understand and summarise the results coming from the full simulation. The laser field will create electron-hole pairs, mainly by promoting electrons from band v2 to band c1. However,

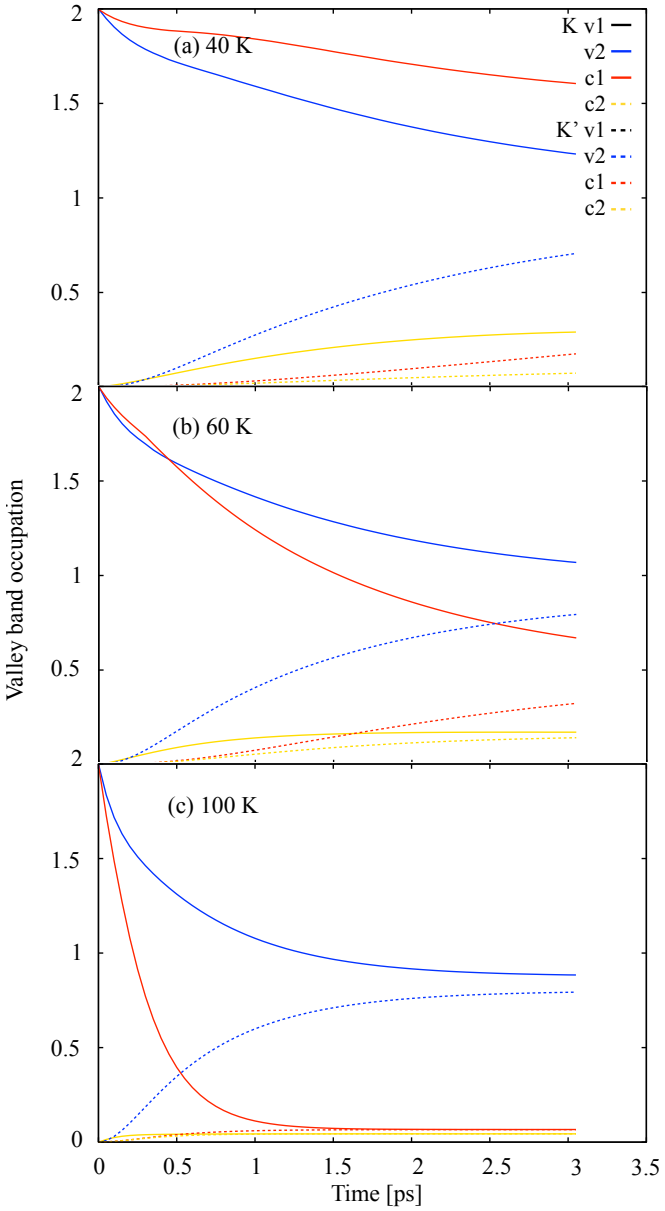

FIG. S9. Time-evolution of valley electron and hole populations for the artificial excited state in which electrons are moved from v2 to c1 at K, at 40K, 60K, and 100K. Full lines represent the populations in the K valley, while dashed lines show the populations of the corresponding band in the K' valley.

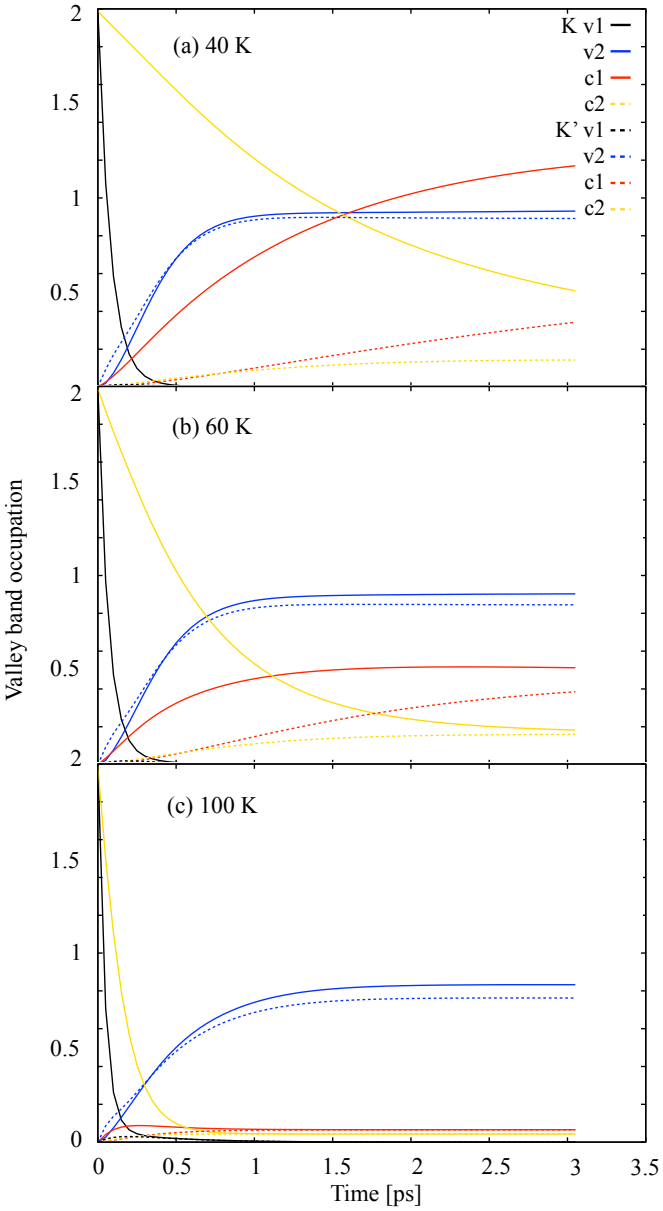

FIG. S10. Time-evolution of valley electron and hole populations for the artificial excited state in which electrons are moved from v1 to c2 at K, at 40K, 60K, and 100K. Full lines represent the populations in the K valley, while dashed lines show the populations of the corresponding band in the K' valley.

due to changes in the screening, the exciton binding energies undergo some renormalisation, thus transferring some electrons from v1 to c2. Carriers will then begin relaxing almost immediately after excitation, due to their interaction with phonons. At low temperatures holes relax faster than electrons, which remain trapped in band c1 at the K valley, either because their were placed there by the laser, or because their underwent spin-flip after being promoted to band c2[34]. This then results in electrons being the main contributors to the magnetisation at lower temperatures. By increasing the temperature, electrons can scatter faster than holes, spreading through the whole Brillouin zone. The magnetisation's signal inverts, and the sample will remain magnetised for as long there is an imbalance between the hole populations in the two valleys. Our results compare well with the ones of Ref. 32, where the authors have studied the effects of temperature in the time-dependent Kerr signal for WSe_2. In that article, however, there was no study of changes with temperature of the relative speed of scattering of

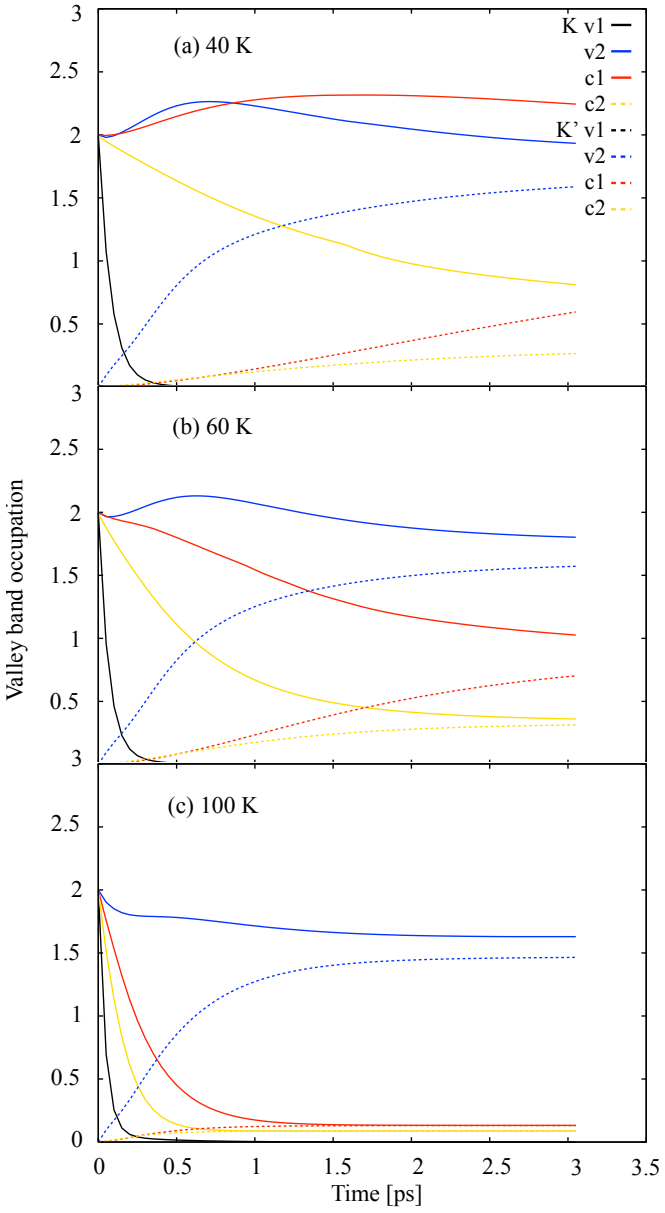

FIG. S11. Time-evolution of valley electron and hole populations for the artificial excited state in which electrons are moved from v2 to c1, and from v1 to c2 at K, at 40K, 60K, and 100K. Full lines represent the populations in the K valley, while dashed lines show the populations of the corresponding band in the K' valley.

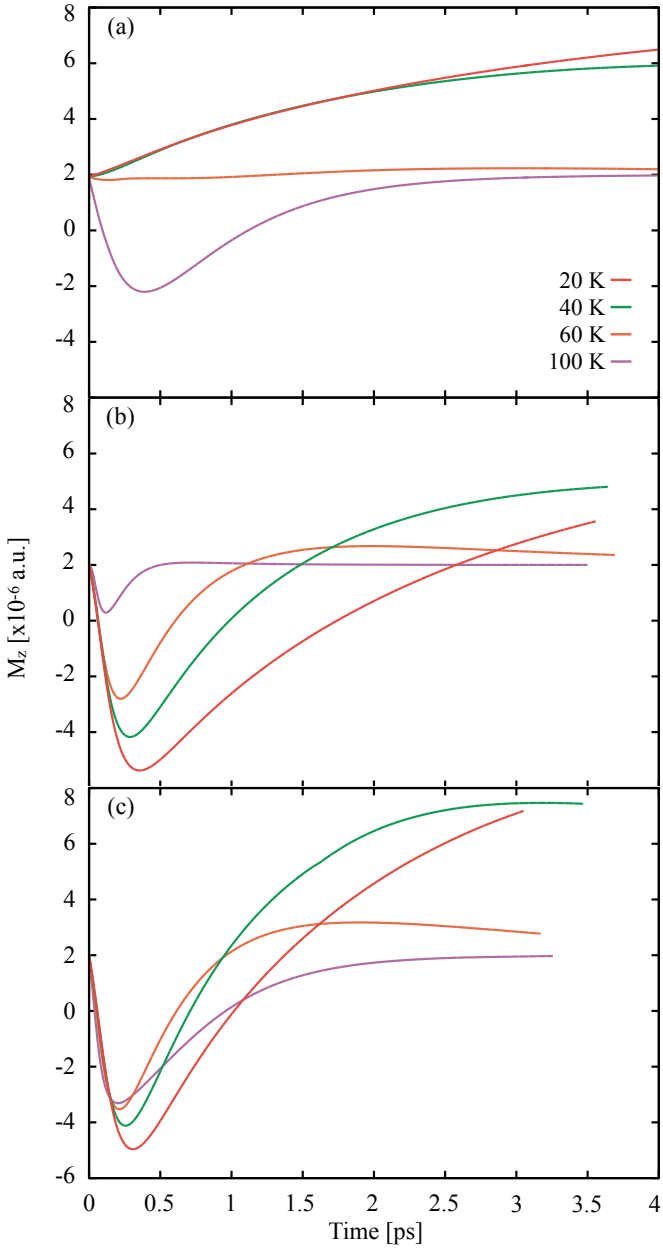

FIG. S12. (Time evolution of the magnetisation for the three test cases where only the electron-phonon interaction was active. (a) electrons moved from v2 to c1; (b) electrons moved from v1 to c2; (c) both transitions.

electrons and holes due to phonons, or as to how this would reflect in the changes in the magnetisation's signal. With respect to our system, the one used in Ref. 32 has a different spin composition of the bands at K' (and K). In the $MoSe_2$ case, at K bands are ordered as (down, up, up, down), while in WSe_2 the ordering is (down, up, down, up). If we were to label the bands in the same way, with respect to their energies, a circularly polarised laser creates electron-hole pairs in K by promoting electrons from v2 to c2. Taking from our observations, this would mean that at low temperatures the dominant relaxation process for electrons would be phonon-induced spin flip, trapping them in band c1 at K'. We have shown that the electron-phonon (and also hole-phonon) interaction can account for the sign changes in the Kerr-signal with temperature and have explained which mechanisms (inter and intra-valley scattering) drive those changes. We are in the same regime as Ref. 32, i.e. low intensity of the laser pump, which means that we can safely ignore the electron-hole exchange mechanism, as this is only dominant at high exciton densities and is mostly temperature

independent (the temperature will contribute only via the thermal distribution of excitons).

[1] Martinez-Martin, D.; Longuinhos, R.; Izquierdo, J. G.; Marele, A.; Alexandre, S. S.; Jaafar, M.; Gómez-Rodríguez, J. M.; Banares, L.; Soler, J. M.; Gomez-Herrero, J. Atmospheric contaminants on graphitic surfaces. *Carbon* **2013**, *61*, 33 – 39.

[2] Kozbial, A.; Gong, X.; Liu, H.; Li, L. Understanding the Intrinsic Water Wettability of Molybdenum Disulfide (MoS2). *Langmuir* **2015**, *31*, 8429–8435.

[3] Ulbricht, H.; Zacharia, R.; Cindir, N.; Hertel, T. Thermal desorption of gases and solvents from graphite and carbon nanotube surfaces. *Carbon* **2006**, *44*, 2931–2942.

[4] Schmalbuch, K.; Göbbels, S.; Schäfers, P.; Rodenbücher, C.; Schlammes, P.; Schäpers, T.; Lepsa, M.; Güntherodt, G.; Beschoten, B. Two-Dimensional Optical Control of Electron Spin Orientation by Linearly Polarized Light in InGaAs. *Phys. Rev. Lett.* **2010**, *105*, 246603.

[5] Kuhlen, S.; Ledesch, R.; de Winter, R.; Althammer, M.; Gönnenwein, S. T. B.; Opel, M.; Gross, R.; Wassner, T. A.; Brandt, M. S.; Beschoten, B. Unambiguous determination of spin dephasing times in ZnO by time-resolved magneto-optical pump-probe experiments. *Phys. Status Solidi (b)* **2014**, *251*, 1861–1871.

[6] Volmer, F.; Pissinger, S.; Ersfeld, M.; Kuhlen, S.; Stampfer, C.; Beschoten, B. Intervalley dark trion states with spin lifetimes of 150 ns in WSe_2. *Phys. Rev. B* **2017**, *95*, 235408.

[7] Crooker, S. A.; Awschalom, D. D.; Baumberg, J. J.; Flack, F.; Samarth, N. Optical spin resonance and transverse spin relaxation in magnetic semiconductor quantum wells. *Phys. Rev. B* **1997**, *56*, 7574–7588.

[8] McCormick, E. J.; Newburger, M. J.; Luo, Y. K.; McCreary, K. M.; Singh, S.; Martin, I. B.; Cichewicz, E. J., Jr.; Jonker, B. T.; Kawakami, R. K. Imaging spin dynamics in monolayer WS2 by time-resolved Kerr rotation microscopy. *2D Mater.* **2017**, *5*, 011010.

[9] Zhou, Y.; Scuri, G.; Wild, D. S.; High, A. A.; Dibos, A.; Jauregui, L. A.; Shu, C.; De Greve, K.; Pistunova, K.; Joe, A. Y.; Taniguchi, T.; Watanabe, K.; Kim, P.; Lukin, M. D.; Park, H. Probing dark excitons in atomically thin semiconductors via near-field coupling to surface plasmon polaritons. *Nat. Nanotechnol.* **2017**, *12*, 856.

[10] Sidler, M.; Back, P.; Cotlet, O.; Srivastava, A.; Fink, T.; Kroner, M.; Demler, E.; Imamoglu, A. Fermi polaron-polaritons in charge-tunable atomically thin semiconductors. *Nat. Phys.* **2016**, *13*, 255.

[11] Jones, A. M.; Yu, H.; Ghimire, N. J.; Wu, S.; Aivazian, G.; Ross, J. S.; Zhao, B.; Yan, J.; Mandrus, D. G.; Xiao, D.; Yao, W.; Xu, X. Optical generation of excitonic valley coherence in monolayer WSe2. *Nat. Nanotechnol.* **2013**, *8*, 634.

[12] Island, J. O.; Kuc, A.; Diependaal, E. H.; Bratschitsch, R.; van der Zant, H. S. J.; Heine, T.; Castellanos-Gomez, A. Precise and reversible band gap tuning in single-layer MoSe2 by uniaxial strain. *Nanoscale* **2016**, *8*, 2589.

[13] Zhu, C. R.; Wang, G.; Liu, B. L.; Marie, X.; Qiao, X. F.; Zhang, X.; Wu, X. X.; Fan, H.; Tan, P. H.; Amand, T.; Urbaszek, B. Strain tuning of optical emission energy and polarization in monolayer and bilayer MoS_2. *Phys. Rev. B* **2013**, *88*, 121301.

[14] Conley, H. J.; Wang, B.; Ziegler, J. I.; Haglund, R. F.; Pantelides, S. T.; Bolotin, K. I. Bandgap Engineering of Strained Monolayer and Bilayer MoS2. *Nano Lett.* **2013**, *13*, 3626–3630.

[15] Wierzbowski, J.; Klein, J.; Sigger, F.; Straubinger, C.; Kremser, M.; Taniguchi, T.; Watanabe, K.; Wurstbauer, U.; Holleitner, A. W.; Kaniber, M.; Müller, K.; Finley, J. J. Direct exciton emission from atomically thin transition metal dichalcogenide heterostructures near the lifetime limit. *Sci. Rep.* **2017**, *7*, 12383.

[16] Ajayi, O. A.; Ardelean, J. V.; Shepard, G. D.; Wang, J.; Antony, A.; Taniguchi, T.; Watanabe, K.; Heinz, T. F.; Strauf, S.; Zhu, X.-Y.; Hone, J. C. Approaching the intrinsic photoluminescence linewidth in transition metal dichalcogenide monolayers. *2D Mater.* **2017**, *4*, 031011.

[17] Cadiz, F. et al. Ultra-low power threshold for laser induced changes in optical properties of 2D molybdenum dichalcogenides. *2D Mater.* **2016**, *3*, 045008.

[18] Ye, J.; Yan, T.; Niu, B.; Li, Y.; Zhang, X. Nonlinear dynamics of trions under strong optical excitation in monolayer MoSe2. *Sci. Rep.* **2018**, *8*, 2389.

[19] Jadczak, J.; Kutrowska-Girzycka, J.; Kapuściński, P.; Huang, Y. S.; Wójs, A.; Bryja, L. Probing of free and localized excitons and trions in atomically thin WSe2, WS2, MoSe2 and MoS2 in photoluminescence and reflectivity experiments. *Nanotechnology* **2017**, *28*, 395702.

[20] Ross, J. S.; Wu, S.; Yu, H.; Ghimire, N. J.; Jones, A. M.; Aivazian, G.; Yan, J.; Mandrus, D. G.; Xiao, D.; Yao, W.; Xu, X. Electrical control of neutral and charged excitons in a monolayer semiconductor. *Nat. Commun.* **2013**, *4*, 1474–.

[21] Chakraborty, C.; Goodfellow, K. M.; Vamivakas, A. N. Localized emission from defects in MoSe2 layers. *Opt. Mater. Express* **2016**, *6*, 2081–2087.

[22] Han, H.-V.; Lu, A.-Y.; Lu, L.-S.; Huang, J.-K.; Li, H.; Hsu, C.-L.; Lin, Y.-C.; Chiu, M.-H.; Suenaga, K.; Chu, C.-W.; Kuo, H.-C.; Chang, W.-H.; Li, L.-J.; Shi, Y. Photoluminescence Enhancement and Structure Repairing of Monolayer MoSe2 by Hydrohalic Acid Treatment. *ACS Nano* **2016**, *10*, 1454–1461.

[23] Wang, G.; Palleau, E.; Amand, T.; Tongay, S.; Marie, X.; Urbaszek, B. Polarization and time-resolved photoluminescence spectroscopy of excitons in MoSe2 monolayers. *Appl. Phys. Lett.* **2015**, *106*, 112101.

[24] Hamann, D. R. Optimized norm-conserving Vanderbilt pseudopotentials. *Phys. Rev. B* **2013**, *88*, 085117.

[25] van Setten, M. J.; Giantomassi, M.; Bousquet, E.; Verstraete, M. J.; Hamann, D. R.; Gonze, X.; Rignanese, G.-M. The PseudoDojo: Training and grading a 85 element optimized norm-conserving pseudopotential table. *Comput. Phys. Commun.* **2018**, *226*, 39–54.

[26] Sangalli, D. et al. Many-body perturbation theory calculations using the yambo code. *Journal of Physics: Condensed Matter* **2019**,

[27] de Melo, P. M. M. C.; Marini, A. Unified theory of quantized electrons, phonons, and photons out of equilibrium: A simplified ab initio approach based on the generalized Baym-

Kadanoff ansatz. *Phys. Rev. B* **2016**, *93*, 155102.
[28] Marini, A. Competition between the electronic and phonon–mediated scattering channels in the out–of–equilibrium carrier dynamics of semiconductors: an ab-initio approach. *J. Phys. Conf. Ser.* **2013**, *427*, 012003.
[29] Attaccalite, C.; Grüning, M.; Marini, A. Real-time approach to the optical properties of solids and nanostructures: Time-dependent Bethe-Salpeter equation. *Phys. Rev. B* **2011**, *84*, 245110.
[30] Perfetto, E.; Sangalli, D.; Marini, A.; Stefanucci, G. Nonequilibrium Bethe-Salpeter equation for transient photoabsorption spectroscopy. *Phys. Rev. B* **2015**, *92*, 205304.
[31] The dipolar approximation is well justified in this situation, since the wavelength of the laser is much larger than the dimensions of the unit cell.
[32] Molina-Sánchez, A.; Sangalli, D.; Wirtz, L.; Marini, A. Ab Initio Calculations of Ultrashort Carrier Dynamics in Two-Dimensional Materials: Valley Depolarization in Single-Layer WSe2. *Nano Lett.* **2017**, *17*, 4549.
[33] The differences in the seemingly asymptotic values for hole population in both valleys are a result from hole states being populated outside the integration area used to compute the valley band populations.
[34] Note that the spin-flip transition is allowed because carriers transition first to states around K', which are not pure spin states. This process is very fast. See the file dynamics-V2toC1.mov for a side-by-side comparison of the carrier dynamics for the V2 to C1 transition at 40 K and 60 K.